


Resonant mode conversion in partially parity-time-symmetric waveguidesDongdong Wang¹, Yan Wang^{2,*} and Lu Li^{1,2,†}¹*Institute of Theoretical Physics, State Key Laboratory of Quantum Optics and Quantum Optics Devices, Shanxi University, Taiyuan 030006, China*²*College of Physics and Electronics Engineering, Shanxi University, Taiyuan 030006, China* (Received 8 August 2023; revised 1 November 2023; accepted 24 January 2024; published 13 February 2024)

Resonant mode conversions in partially parity-time (\mathcal{PT})-symmetric multimode waveguides are investigated. First, the symmetry breaking and degeneracy splitting of linear eigenmodes are found numerically and analytically. Moreover, mode conversions in the nonconservative system are demonstrated using longitudinally periodic modulation of the complex refractive index. The results show that, under the resonance condition, conversions between the unbroken modes with the same topological charge can occur, with conversion frequency being presented analytically. Finally, the influence of nonlinear effects on the resonant mode conversions is also discussed. It is found that the mode conversions depend on the dynamic equilibrium of the modes in nonlinear media, resulting in the conversions between the quadrupole modes in self-focusing medium, and the basic modes with ring structure in defocusing medium can be achieved. These results are beneficial for our further understanding of mode conversions in complex waveguides and can be applied to manipulation of the optical beam.

DOI: [10.1103/PhysRevA.109.023515](https://doi.org/10.1103/PhysRevA.109.023515)**I. INTRODUCTION**

Parity-time (\mathcal{PT}) symmetric systems have a remarkable feature: the transition from a real to a complex eigenvalue spectrum, referred to as \mathcal{PT} -symmetry breaking, occurs at a critical depth of the imaginary part of the potential [1,2]. This transition manifests itself in the qualitative modification of wave evolution. In optics, \mathcal{PT} -symmetric systems can be realized by involving symmetric index guiding and an anti-symmetric gain/loss profile and can support guided modes with constant power upon propagation [3–7]. So far, a number of novel phenomena in optical \mathcal{PT} -symmetric systems have been reported, including switching operations, unidirectional dynamics, nonreciprocal soliton scattering, asymmetric amplification, jamming anomaly, photon-assisted tunneling, and so on [8–19]. Furthermore, the concept of \mathcal{PT} symmetry has been extended to fractional systems, photonics, and multimode fiber systems [20–25]. At the same time, in multi-dimensions, symmetry breaking of solitons, stability of vortex solitons, and topological states in partially \mathcal{PT} -symmetric potentials have also been investigated [26–31]. Here, the partial \mathcal{PT} symmetry means that the complex potential V is invariant under complex conjugation and reflection in a single spatial direction. In two-dimensions, it satisfies $V^*(x, y) = V(-x, y)$ or $V^*(x, y) = V(x, -y)$ [26].

In the field of optics, Rabi oscillations are manifested as resonant mode conversions. The longitudinally periodic modulation of the refractive index acts as an ac field, resulting in various phenomena such as parametric amplification, the inhibition of light tunneling, and the realization of optical iso-

lation [32–35]. Notably, there exists a mathematical analogy between the stimulated mode conversion process and Rabi flopping, which refers to periodic transitions between two stationary states of a quantum system driven by a resonant external field [36–38]. In recent years, Rabi oscillations have been widely investigated in a variety of optical and photonic systems, including fibers [39,40], multimode waveguides [41–43], coupled waveguides [44], waveguide arrays [45,46], \mathcal{PT} -symmetry waveguides [47], and two-dimensional modal structures [48,49]. Additionally, Rabi oscillations of topological edge states and resonant mode conversions in the fractional Schrödinger equation have been studied [50–52]. Recently, Rabi oscillations of azimuthons in weakly nonlinear waveguides with weak longitudinally periodic modulation of the refractive index and nonlinearity have been investigated [53,54]. However, degeneracy splitting and resonant mode conversion in partially \mathcal{PT} symmetric multimode waveguide has not been reported yet. Degeneracy splitting in this context refers to the occurrence of the division of degenerate modes into two distinct nondegenerate modes, characterized by differing topological structure, when gain/loss is introduced.

In this paper, we investigate resonant mode conversions in partially \mathcal{PT} -symmetric multimode waveguides under the action of longitudinal modulation. First, the characteristics of eigenmodes in a linear regime are discussed numerically and analytically, including symmetry breaking and degeneracy splitting. Moreover, with the aid of resonant coupled mode theory with a biorthogonality condition, mode conversions are demonstrated. The results show that, under the resonance condition, conversions between unbroken modes with the same topological charge and equal parity can occur. Finally, the influence of nonlinear effects on mode conversions is investigated. The results show that in a self-focusing medium, the sine modes can be converted and the basic modes cannot

*Annie@sxu.edu.cn

†llz@sxu.edu.cn

undergo a conversion. Conversely, in a defocusing medium, the basic modes can be converted and the sine modes cannot.

The paper is organized as follows. In the next section, the model and eigenmodes in a linear regime are presented. Under resonant longitudinal modulation, mode conversion in a linear regime is discussed in Sec. III. In Sec. IV, the influence of nonlinear effects on mode conversion is studied. The main results of the paper are summarized in Sec. V.

II. MODEL AND EIGENMODES IN A LINEAR REGIME

We consider light propagation in a multimode waveguide, which can be governed by the nonlinear Schrödinger equation as follows:

$$i \frac{\partial \psi}{\partial z} = -\frac{1}{2} \left(\frac{\partial^2}{\partial x^2} + \frac{\partial^2}{\partial y^2} \right) \psi - V(x, y, z) \psi - \sigma |\psi|^2 \psi. \quad (1)$$

Here, $\psi = \psi(x, y, z)$ is the dimensionless field amplitude, x and y are the transverse coordinates normalized by the characteristic scale r_0 , and z is the longitudinal coordinate normalized by $k_0 r_0^2$. The wave number in the medium is denoted by $k_0 = 2\pi n_b / \lambda_0$, where n_b is the refractive index and λ_0 is the wavelength in vacuum. σ is the nonlinear Kerr coefficient. $V(x, y, z) = R(x, y, z) + iI(x, y, z)$ is a complex potential affecting the propagation of the laser radiation. Its real part describes the refractive index profile and the imaginary part is the gain/loss distribution.

In this study, we consider a harmonic non-Hermitian modulation along a super Gaussian multimode fiber by the simultaneous modulation of the refractive index and the gain/loss. Such modulations may be induced by doping the fiber core, modulating the fiber core radius, and introducing some absorption, scattering, or transmission losses [25]. The form of modulations are $R(x, y, z) = p_r V_r [1 + \mu \sin(\Omega z)]$ and $I(x, y, z) = p_i V_i [1 + \mu \sin(\Omega z + \phi)]$, where $V_r = \exp[-(x^2 + y^2)^5 / w^{10}]$ and $V_i = V_r \sin(\pi x / w) \sin(\pi y / w)$, with w being its width. Here, the parameter $p_r = \delta n k_0^2 r_0^2 / n_b$ is proportional to the real variation of the refractive index, p_i stands for the gain/loss strength, and ϕ is the possible phase shift between the harmonic modulation of the refractive index and gain/loss. The real part $R(x, y, z)$ is symmetric in the transverse direction, while the imaginary part $I(x, y, z)$ is antisymmetric with respect to x and y , respectively, constructing a partially parity-time-symmetric complex waveguide [26]. Both $R(x, y, z)$ and $I(x, y, z)$ are harmonically modulated with the frequency Ω and the amplitude $\mu \ll \Omega$ in the longitudinal direction. Figure 1(a) depicts the distribution plots of V_r and V_i respectively. For $r_0 = 16 \mu\text{m}$ and light beams at the wavelength $\lambda_0 = 800 \text{ nm}$ propagating in fused silica, a waveguide depth $p_r = 200$ corresponds to a refractive index contrast of $\delta n \sim 9 \times 10^{-3}$, the distance $z = 1$ corresponds to a propagation distance of 2.8 mm, and $|\psi|^2 = 1$ corresponds to a peak intensity of $I_0 \sim 1.5 \times 10^{15} \text{ W/m}^2$, assuming a nonlinear coefficient of $n_2 = 3 \times 10^{-20} \text{ m}^2/\text{W}$ [53].

First, we consider the linear version of Eq. (1) without the longitudinal modulation, i.e., $\sigma = 0$ and $\mu = 0$, which supports the linear eigenmodes in the complex waveguide.

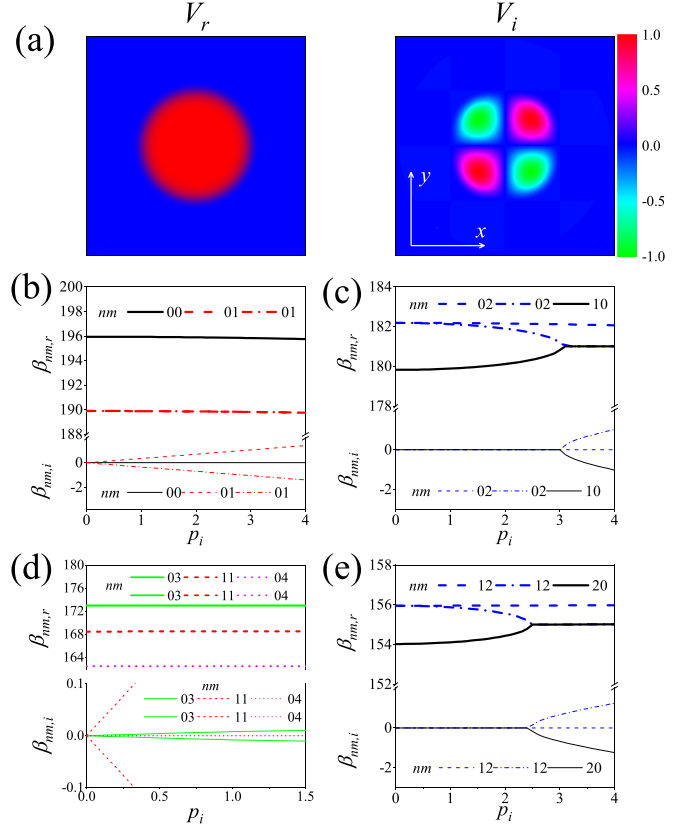


FIG. 1. (a) Diagram of the complex potential. (b)–(e) Dependence of the real parts $\beta_{nm,r}$ and the imaginary parts $\beta_{nm,i}$ of the propagation constants on the gain/loss strength p_i . Based on the arrangement in descending order of β_{nm} , in the absence of gain/loss ($p_i = 0$), they correspond to the following modes: the first-order basic mode \tilde{u}_{00} , the first-order degenerate dipole modes $\tilde{u}_{01,c}$ and $\tilde{u}_{01,s}$, the first-order degenerate quadrupole modes $\tilde{u}_{02,c}$ and $\tilde{u}_{02,s}$, the second-order basic mode \tilde{u}_{10} , the first-order degenerate hexapole modes $\tilde{u}_{03,c}$ and $\tilde{u}_{03,s}$, the second-order degenerate dipole modes $\tilde{u}_{11,c}$ and $\tilde{u}_{11,s}$, the first-order degenerate octopole modes $\tilde{u}_{04,c}$ and $\tilde{u}_{04,s}$, the second-order degenerate quadrupole modes $\tilde{u}_{12,c}$ and $\tilde{u}_{12,s}$, and the third-order basic mode \tilde{u}_{20} . Here, $\sigma = \mu = 0$, $p_r = 200$, and $w = 1$.

The linear eigenmodes with the propagation constant β are sought for in the usual form

$$\psi(x, y, z) = u(x, y) \exp(i\beta z), \quad (2)$$

with the linear eigenmode $u(x, y)$ satisfying the following equation:

$$\beta u = -\mathcal{H}u. \quad (3)$$

Here, $\mathcal{H} = \mathcal{H}_0 - ip_i V_i$ is a non-Hermitian operator, where $\mathcal{H}_0 = -(1/2)\nabla_{\perp}^2 - p_r V_r$ is Hermitian. Equation (3) is a linear steady-state eigenvalue problem of Eq. (1) when σ and μ are set to zero. Especially, as $p_i = 0$, it is an eigenvalue problem for the Hermitian operator \mathcal{H}_0 and exists as a series of stationary vortex solutions, $\tilde{u}_{nm} = R_{nm}(r) \exp(im\theta)$, with the real propagation constant $\tilde{\beta}_{nm}$, where $R_{nm}(r)$ is the radial wave function, m is the topological charge, and n is the radial node number, which are integers [53,54]. In the case of $m \neq 0$, the real and imaginary parts of \tilde{u}_{nm} provide two degenerate

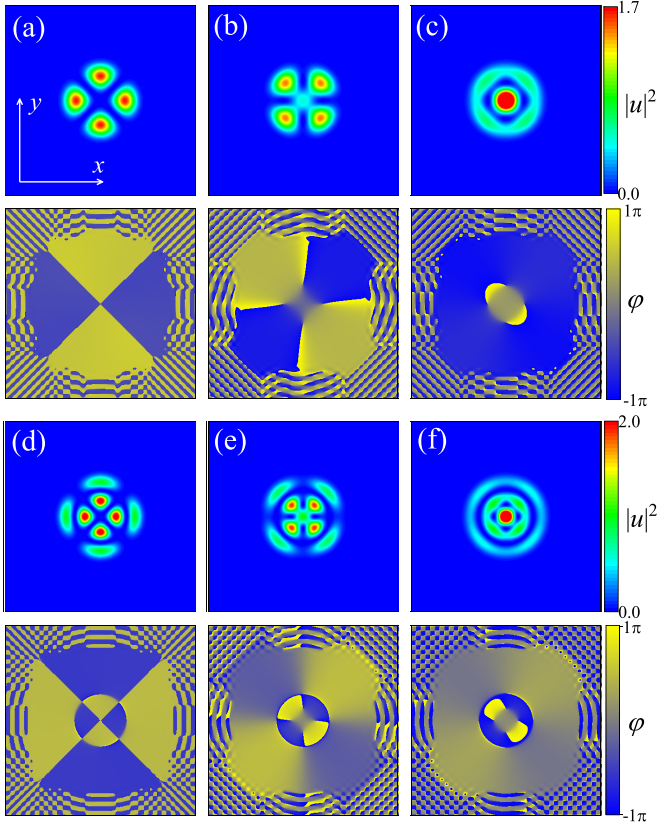


FIG. 2. Intensity and phase distributions of the corresponding linear eigenmodes at $p_i = 2$. (a) The cosine mode $u_{02,c}$, (b) the sine mode $u_{02,s}$, (c) the adjacent basic mode u_{10} , (d) the cosine mode $u_{12,c}$, (e) the sine mode $u_{12,s}$, and (f) the adjacent basic mode u_{20} . Here, the parameters are the same as those in Fig. 1.

$(n + 1)$ th-order $2|m|$ -pole linear eigenmodes with the propagation constant $\tilde{\beta}_{nm}$ as follows:

$$\tilde{u}_{nm,c} = R_{nm}(r) \cos(m\theta), \quad (4)$$

$$\tilde{u}_{nm,s} = R_{nm}(r) \sin(m\theta). \quad (5)$$

Here, for convenience, we refer to $\tilde{u}_{nm,c}$ and $\tilde{u}_{nm,s}$ as the cosine and sine eigenmodes, respectively. Note that when $m = 0$, the eigenmodes are nondegenerate and are called basic modes. In general, Eq. (3) is an eigenvalue problem for the non-Hermitian operator \mathcal{H} and its eigenmode $u_{nm}(x, y)$, with the propagation constant (generally also complex) $\beta_{nm} = \beta_{nm,r} + i\beta_{nm,i}$, that can be solved using the plane-wave expansion method [50,55].

Figures 1(b)–1(e) present examples to demonstrate the dependence of the real parts $\beta_{nm,r}$ and the imaginary parts $\beta_{nm,i}$ of propagation constants on the gain/loss strength p_i . With the presence of gain/loss ($p_i \neq 0$), the propagation constants of eigenmodes exhibit different characteristics. For instance, the propagation constants of eigenmodes $u_{nm,c}$ and $u_{nm,s}$, with $nm = 01, 03$, and 11 , have equal real parts but opposite imaginary parts, as shown by the red curves in Fig. 1(b) and by the green and red curves in Fig. 1(d). This indicates that the degeneracy and symmetry of these eigenmodes are broken with the appearance of gain/loss.

For the basic mode u_{00} and octupole modes $u_{04,c}$ and $u_{04,s}$, the imaginary parts of their propagation constants are always equal to zero as p_i increases, and the real parts remain unchanged, as shown by the black curves in Fig. 1(b) and by the magenta curves in Fig. 1(d). Hence, their symmetry and degeneracy remain even in the presence of gain/loss.

As for quadrupole modes $u_{02,c}$ and $u_{02,s}$, as well as $u_{12,c}$ and $u_{12,s}$, the real parts of the propagation constants split as p_i increases, while the imaginary parts remain zero, until the split parts merge with the propagation constants of the adjacent basic modes u_{10} and u_{20} at critical points $p_i = p_i^{cr} \approx 3.0378$ and 2.4632 , respectively, as shown in Figs. 1(c) and 1(e). Thus, when $p_i < p_i^{cr}$, their symmetry remains but the degeneracy is split. Their intensity and phase distributions at $p_i = 2$ ($< p_i^{cr}$) are shown in Fig. 2. It can be seen that the first-order and second-order cosine quadrupole modes maintain their profiles and topological charge, as shown in Figs. 2(a) and 2(d). However, the split sine quadrupole modes exhibit a bulge in the central region, so their topological charge becomes zero [see Figs. 2(b) and 2(e)], and the ring structures of the adjacent second-order and third-order basic modes are dividing, as shown in Figs. 2(c) and 2(f), eventually resulting in their profiles tending to be similar to each other.

In order to illustrate these characteristics of the symmetry breaking and degeneracy splitting, we construct the matrix representation H for the complex operator \mathcal{H} by defining the matrix element $H_{ab} = \tilde{\beta}_a \delta_{ab} - ip_i \tilde{V}_i^{ab}$, where $\tilde{V}_i^{ab} = \langle \tilde{u}_a | V_i | \tilde{u}_b \rangle$, with \tilde{u}_a and \tilde{u}_b taking all possible modes for \mathcal{H}_0 . Note that the matrix element H_{ab} can be determined by the propagation constants and modes for \mathcal{H}_0 and the imaginary part V_i of the potential. Obviously, $\tilde{V}_i^{aa} = \iint \tilde{u}_{nm,c}^2 V_i dx dy$ (or $\iint \tilde{u}_{nm,s}^2 V_i dx dy$) = 0 due to the antisymmetry of V_i . The other values of \tilde{V}_i^{ab} can be obtained by numerical calculation and the partial list is as follows:

$\tilde{V}_i^{ab} \tilde{u}_b$	$\tilde{u}_{n'0}$	$\tilde{u}_{n'1,c}$	$\tilde{u}_{n'1,s}$	$\tilde{u}_{n'2,c}$	$\tilde{u}_{n'2,s}$	$\tilde{u}_{n'3,c}$	$\tilde{u}_{n'3,s}$	$\tilde{u}_{n'4,c}$	$\tilde{u}_{n'4,s}$
$\tilde{u}_{n'0}$	0	0	0	0	N	0	0	0	0
$\tilde{u}_{n'1,c}$	0	0	N	0	0	0	N	0	0
$\tilde{u}_{n'1,s}$	0	N	0	0	0	N	0	0	0
$\tilde{u}_{n'2,c}$	0	0	0	0	0	0	0	0	N
$\tilde{u}_{n'2,s}$	N	0	0	0	0	0	0	N	0
$\tilde{u}_{n'3,c}$	0	0	N	0	0	0	N	0	0
$\tilde{u}_{n'3,s}$	0	N	0	0	0	N	0	0	0
$\tilde{u}_{n'4,c}$	0	0	0	0	N	0	0	0	0
$\tilde{u}_{n'4,s}$	0	0	0	N	0	0	0	0	0

where n and n' are integers, and ‘‘N’’ indicates that the value of \tilde{V}_i^{ab} is nonzero. Thus, the dependence of the propagation constants for \mathcal{H} on the gain/loss strength p_i can be described by eigenvalues of H or its submatrix [28].

Here, we consider the cases shown in Figs. 1(b), 1(c), and 1(e). Since three modes, $\tilde{u}_{1,2,3}$, for \mathcal{H}_0 are involved, they can be illustrated using a 3×3 submatrix. In these cases, the corresponding propagation constants $\tilde{\beta}_{1,2,3}$ have two different situations. One is $\tilde{\beta}_1 > \tilde{\beta}_2 = \tilde{\beta}_3$ and the other is $\tilde{\beta}_1 = \tilde{\beta}_2 > \tilde{\beta}_3$. Specifically, in Fig. 1(b), $\tilde{u}_1 = \tilde{u}_{00}$ is a basic mode, $\tilde{u}_2 = \tilde{u}_{01,c}$ and $\tilde{u}_3 = \tilde{u}_{01,s}$ are degenerate modes, and the corresponding

propagation constants are $\tilde{\beta}_1 = \tilde{\beta}_{00}$ and $\tilde{\beta}_2 = \tilde{\beta}_3 = \tilde{\beta}_{01}$, respectively. In Figs. 1(c) and 1(e), $\tilde{u}_1 = \tilde{u}_{02,c}$ ($\tilde{u}_{12,c}$) and $\tilde{u}_2 = \tilde{u}_{02,s}$ ($\tilde{u}_{12,s}$) are degenerate modes, $\tilde{u}_3 = \tilde{u}_{10}$ (\tilde{u}_{20}) is a basic mode, and the corresponding propagation constants are $\tilde{\beta}_1 = \tilde{\beta}_2 = \tilde{\beta}_{02}$ and $\tilde{\beta}_3 = \tilde{\beta}_{10}$ ($\tilde{\beta}_1 = \tilde{\beta}_2 = \tilde{\beta}_{12}$ and $\tilde{\beta}_3 = \tilde{\beta}_{20}$), respectively. In either case, there are $\tilde{V}_i^{12} = \tilde{V}_i^{13} = 0$ (see the table above). Thus, one can obtain a 3×3 submatrix representation of H as follows:

$$H_s = \begin{bmatrix} \tilde{\beta}_1 & 0 & 0 \\ 0 & \tilde{\beta}_2 & -ip_i \tilde{V}_i^{23} \\ 0 & -ip_i \tilde{V}_i^{32} & \tilde{\beta}_3 \end{bmatrix}. \quad (6)$$

Its eigenvalues are given by $\beta_1 = \tilde{\beta}_1$ and $\beta_{2,3} = (\tilde{\beta}_2 + \tilde{\beta}_3)/2 \pm [(\tilde{\beta}_2 - \tilde{\beta}_3)^2/4 - p_i^2 |\tilde{V}_i^{23}|^2]^{1/2}$. Obviously, they can be reduced to $\beta_1 = \tilde{\beta}_1$, $\beta_2 = \tilde{\beta}_2$, and $\beta_3 = \tilde{\beta}_3$ in the absence of gain/loss.

For the case of Fig. 1(b), the propagation constants corresponding to eigenmodes u_{00} , $u_{01,c}$, and $u_{01,s}$ are given by $\beta_{00} = \tilde{\beta}_{00}$, $\beta_{01,c} = \tilde{\beta}_{01} + ip_i |\tilde{V}_i^{23}|$, and $\beta_{01,s} = \tilde{\beta}_{01} - ip_i |\tilde{V}_i^{23}|$, where $\tilde{V}_i^{23} = \langle \tilde{u}_{01,c} | V_i | \tilde{u}_{01,s} \rangle \neq 0$. This means that with the presence of gain/loss, the first-order basic mode remains unchanged, as shown by the black curves in Fig. 1(b), and the cosine and sine dipole eigenmodes are broken due to $\tilde{V}_i^{23} \neq 0$, as shown by the red curves in Fig. 1(b).

For the cases shown in Figs. 1(c) and 1(e), we only provide a detailed explanation of Fig. 1(c). In this case, the propagation constants corresponding to eigenmodes $u_{02,c}$, $u_{02,s}$, and u_{10} are determined by $\beta_{02,c} = \tilde{\beta}_{02}$, $\beta_{02,s} = (\tilde{\beta}_{02} + \tilde{\beta}_{10})/2 + [(\tilde{\beta}_{02} - \tilde{\beta}_{10})^2/4 - p_i^2 |\tilde{V}_i^{23}|^2]^{1/2}$, and $\beta_{10} = (\tilde{\beta}_{02} + \tilde{\beta}_{10})/2 - [(\tilde{\beta}_{02} - \tilde{\beta}_{10})^2/4 - p_i^2 |\tilde{V}_i^{23}|^2]^{1/2}$, where $\tilde{V}_i^{23} = \langle \tilde{u}_{02,s} | V_i | \tilde{u}_{10} \rangle \neq 0$. It can be seen that with increasing the gain/loss, the degenerate eigenvalue $\tilde{\beta}_{02}$ splits into $\beta_{02,c}$ and $\beta_{02,s}$, where $\beta_{02,c} = \tilde{\beta}_{02}$ remains unchanged, while $\beta_{02,s}$ decreases and β_{10} increases until they intersect at the critical point $p_i = p_i^{\text{cr}} \equiv (\tilde{\beta}_{02} - \tilde{\beta}_{10})/(2|\tilde{V}_i^{23}|) = 2.9766$. The results are consistent with the numerical results in Fig. 1(c).

Similarly, for the case of Fig. 1(e), the critical point is $p_i^{\text{cr}} = (\tilde{\beta}_{12} - \tilde{\beta}_{20})/(2|\tilde{V}_i^{23}|) = 2.4216$, which is approximately equal to the result obtained from the numerical calculation in Fig. 1(e).

III. CONVERSION BETWEEN LINEAR EIGENMODES

After understanding the characteristics of the linear eigenmodes in the complex waveguide without longitudinal modulation, we investigate the dynamics of these eigenmodes in the presence of longitudinal modulation, where $\mu \neq 0$ and $\sigma = 0$. It was found that during the dynamical evolution of these eigenmodes, conversion between modes with the same topological charge may occur. In the following, we only consider conversion between unbroken quadrupole modes, as well as basic modes.

Figure 3(a) presents an example to demonstrate the conversion between the cosine modes $u_{02,c}$ and $u_{12,c}$ at $p_i = 2$ for $\phi = 0$. It can be seen that under resonant longitudinal modulation with $\Omega = \beta_{02,c} - \beta_{12,c}$, the initially incident mode $u_{02,c}$ undergoes a conversion into the mode $u_{12,c}$ at $z = z_1$ and then returns to its original mode $u_{02,c}$ at $z = z_2$. This completes one cycle of Rabi oscillation.

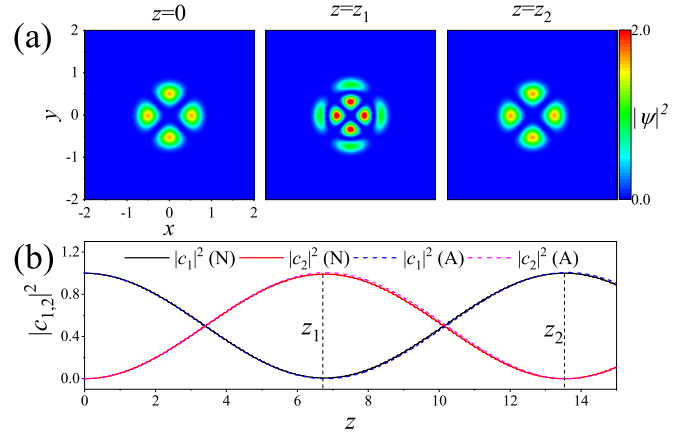


FIG. 3. Conversion between two cosine modes $u_{02,c}$ and $u_{12,c}$ at $p_i = 2$ in the linear regime. (a) Intensity distributions at $z = 0$, z_1 , and z_2 , and (b) corresponding evolution of the weights $|c_{1,2}(z)|^2$, where the solid curves are numerical results, and the dashed curves are analytical results. Here, $z_1 = 6.716$, $z_2 = 13.534$, and $\beta_{02,c} = 182.1574$ and $\beta_{12,c} = 155.9633$ are the eigenvalues of $u_{02,c}$ and $u_{12,c}$, respectively, $\phi = 0$, $\mu = 0.1$, $\sigma = 0$, $\Omega = \beta_{02,c} - \beta_{12,c}$, and the other parameters are the same as those in Fig. 1.

In order to illustrate the mode conversion, we consider a superposition of the two unbroken modes $u_{1,2}(x, y)$ with the same topological charge

$$\psi(x, y, z) = c_1(z)u_1(x, y)e^{i\beta_1 z} + c_2(z)u_2(x, y)e^{i\beta_2 z}, \quad (7)$$

where $\beta_{1,2}$ are the corresponding propagation constants, and $|c_{1,2}(z)|^2$ can be used to account for the weight of each mode and can be calculated by

$$c_1(z) = e^{-i\beta_1 z} \frac{\iint u_1(x, y)\psi(x, y, z)dx dy}{\iint u_1^2(x, y)dx dy},$$

$$c_2(z) = e^{-i\beta_2 z} \frac{\iint u_2(x, y)\psi(x, y, z)dx dy}{\iint u_2^2(x, y)dx dy}. \quad (8)$$

Here, we have made use of the biorthogonality condition in the non-Hermitian system, $\iint u_1(x, y)u_2(x, y)dx dy = 0$, as $p_i \neq 0$ [47,56].

By substituting Eq. (7) into Eq. (1) with $\sigma = 0$, multiplying both sides by $u_1(x, y)$ and $u_2(x, y)$, respectively, integrating over the transverse coordinates, and considering the resonance condition $\Omega = \beta_1 - \beta_2$, we can derive the following system of equations:

$$\frac{dc_1}{dz} = i\mu [p_r V_r^{11} \sin(\Omega z) + ip_i V_i^{11} \sin(\Omega z + \phi)] c_1$$

$$+ i\mu [p_r V_r^{12} \sin(\Omega z) + ip_i V_i^{12} \sin(\Omega z + \phi)] c_2 e^{-i\Omega z},$$

$$\frac{dc_2}{dz} = i\mu [p_r V_r^{21} \sin(\Omega z) + ip_i V_i^{21} \sin(\Omega z + \phi)] c_1 e^{i\Omega z}$$

$$+ i\mu [p_r V_r^{22} \sin(\Omega z) + ip_i V_i^{22} \sin(\Omega z + \phi)] c_2, \quad (9)$$

where $V_r^{ab} = \iint u_a V_r u_b dx dy / \iint u_a^2 dx dy$ and $V_i^{ab} = \iint u_a V_i u_b dx dy / \iint u_a^2 dx dy$, with $a, b = 1$ and 2 . By employing the rotating-wave approximation and neglecting

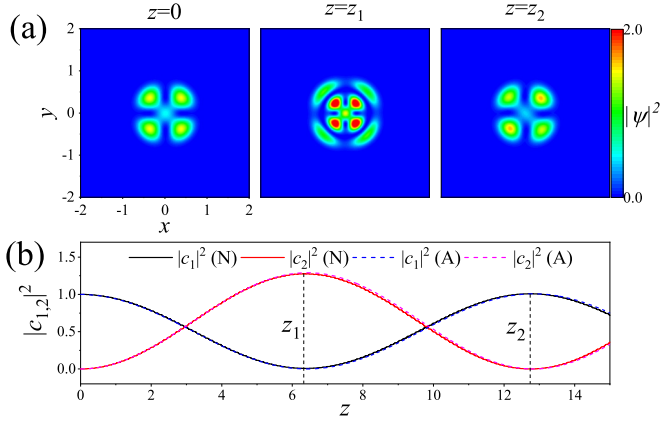


FIG. 4. Conversion between two sine modes $u_{02,s}$ and $u_{12,s}$ at $p_i = 2$ in the linear regime. (a) Intensity distributions at $z = 0$, z_1 , and z_2 , and (b) corresponding evolution of the weights $|c_{1,2}(z)|^2$, where the solid curves are numerical results, and the dashed curves are analytical results. Here, $z_1 = 6.323$, $z_2 = 12.741$, and $\beta_{02,s} = 181.8987$ and $\beta_{12,s} = 155.5644$ are the eigenvalues of $u_{02,s}$ and $u_{12,s}$, respectively, $\phi = 0$, $\mu = 0.1$, $\sigma = 0$, $\Omega = \beta_{02,s} - \beta_{12,s}$, and the other parameters are the same as those in Fig. 1.

the terms containing $e^{\pm i\Omega z}$, $e^{\pm i2\Omega z}$, $e^{\pm i(\Omega z + \phi)}$, and $e^{\pm i(2\Omega z + \phi)}$ [57], Eq. (9) can be simplified as

$$\begin{aligned} \frac{dc_1}{dz} &= \frac{\mu}{2} (p_r V_r^{12} + ip_i e^{i\phi} V_i^{12}) c_2, \\ \frac{dc_2}{dz} &= -\frac{\mu}{2} (p_r V_r^{21} + ip_i e^{-i\phi} V_i^{21}) c_1. \end{aligned} \quad (10)$$

Using Eq. (10), the frequency of mode conversion between the two unbroken modes under resonant modulation is given by

$$\Omega_R = \mu \sqrt{(p_r V_r^{12} + ip_i e^{i\phi} V_i^{12})(p_r V_r^{21} + ip_i e^{-i\phi} V_i^{21})}. \quad (11)$$

Especially, when $p_i = 0$, the result is similar to that in Ref. [41]. From Eq. (10), it can be shown that if Ω_R includes the imaginary part or is equal to zero, then mode conversion does not occur.

Figure 3(b) presents the evolution of weights $|c_{1,2}(z)|^2$ corresponding to the cosine modes shown in Fig. 3(a). Initially, at $z = 0$, we have $c_1(0) = 1$ and $c_2(0) = 0$. As the propagation distance increases, the weight $|c_1(z)|^2$ gradually decreases until it reaches its minimum at $z = z_1$, indicating the occurrence of mode conversion. Subsequently, with further propagation, $|c_1(z)|^2$ increases, while $|c_2(z)|^2$ decreases until it reaches its minimum at $z = z_2$, resulting in the mode returning back to its initial profile. The numerical result for the period is $T_c = z_2 = 13.534$, which is in agreement with the analytical result obtained from Eq. (11), giving $T_c = 2\pi/\Omega_R = 13.5995$.

Furthermore, mode conversion can also be demonstrated between the sine modes $u_{02,s}$ and $u_{12,s}$, as well as the basic modes u_{10} and u_{20} , as shown in Figs. 4 and 5, where the numerical and analytical results of the period are $T_s = 12.741$ and 12.8345 and $T_b = 24.747$ and 24.8663 , respectively. However, it should be noted that mode conversion between $u_{02,c}$ and $u_{12,s}$, as well as $u_{02,s}$ and $u_{12,c}$, does not

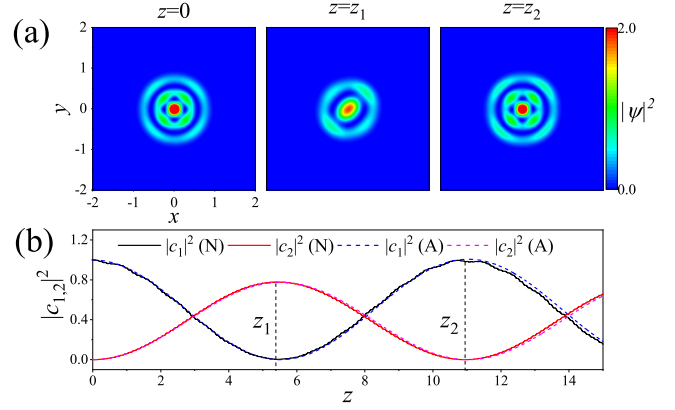


FIG. 5. Conversion between two basic modes u_{20} and u_{10} at $p_i = 2$ in the linear regime. (a) Intensity distributions at $z = 0$, z_1 , and z_2 , and (b) corresponding evolution of the weights $|c_{1,2}(z)|^2$, where the solid curves are numerical results, and the dashed curves are analytical results. Here, $z_1 = 5.383$, $z_2 = 10.946$, and $\beta_{10} = 180.1170$ and $\beta_{20} = 154.4388$ are the eigenvalues of u_{10} and u_{20} , respectively, $\phi = \pi$, $\mu = 0.1$, $\sigma = 0$, $\Omega = \beta_{10} - \beta_{20}$, and the other parameters are the same as those in Fig. 1.

occur due to different topological charges and distinct parities (see Fig. 2).

It should be emphasized that mode conversion may occur at the point where $|c_1(z)|^2$ or $|c_2(z)|^2$ reaches its minimum value (generally, it is equal to zero or approximates to zero). In the nonconservative system under study, the total weight (or power), $|c_1(z)|^2 + |c_2(z)|^2$, may not be equal to 1. For the conversion from low-order modes to high-order modes, the gain of the system plays a dominant role, resulting in the weight being greater than 1, as shown in Fig. 4. Conversely, for the conversion from high-order modes to low-order modes, the loss plays a dominant role, causing its value to be less than 1, as shown in Fig. 5. This feature is distinct from that of a conservative system [41].

The above results indicate that the conversion period T can be determined by $T = 2\pi/\Omega_R$, where Ω_R is given by Eq. (11). Figure 6 shows dependence of the conversion period T on the modulation phase shift ϕ for different gain/loss strengths p_i . From it, one can see that for the cosine modes $u_{02,c}$ and $u_{12,c}$, the parameters ϕ and p_i only have a little effect on the conversion period. However, for the sine modes $u_{02,s}$ and $u_{12,s}$, as well as the basic modes u_{10} and u_{20} , the parameter ϕ has the opposite effect for a given p_i . For the former, ϕ has an inhibitory effect on the conversion period, which reaches its maximum at $\phi = \pi$. On the other hand, for the latter, it plays a facilitating role, and the conversion period reaches its minimum at $\phi = \pi$.

IV. INFLUENCE OF NONLINEAR EFFECT ON LINEAR MODE CONVERSION

In this section, we investigate the influence of the nonlinear effect on mode conversion dynamics. Similarly, we consider a superposition of two unbroken eigenmodes as given in Eq. (7) and numerically calculate the weight of each mode using Eq. (8).

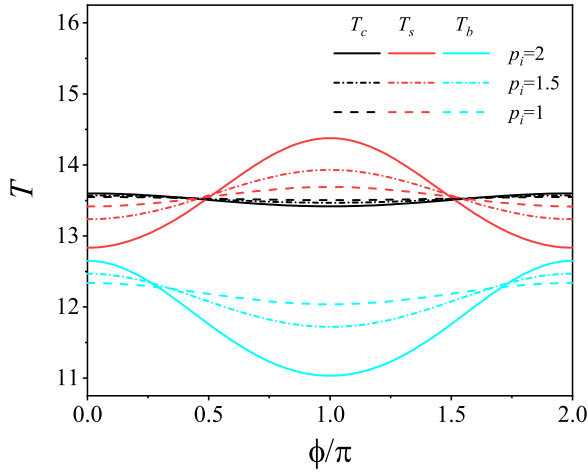


FIG. 6. Relationship of the conversion period T and the modulation phase shift ϕ for different gain/loss strengths p_i , where T_c , T_s , and T_b are the conversion period between the cosine modes $u_{02,c}$ and $u_{12,c}$, the sine modes $u_{02,s}$ and $u_{12,s}$, and the basic modes u_{10} and u_{20} , respectively. Here, $\mu = 0.1$, $\sigma = 0$, and the other parameters are the same as those in Fig. 1.

First, we demonstrate the conversion dynamics of the sine modes $u_{02,s}$ and $u_{12,s}$ under the combined effect of longitudinal modulation and nonlinearity. We start with $u_{02,s}$ as the initial input and allow it to evolve from $z = 0$ to $z = z_1$ in a nonlinear medium without any longitudinal modulation. Then, at $z = z_1$, we introduce longitudinal modulation with a resonant frequency of $\Omega = \beta_{02,s} - \beta_{12,s}$ and let it evolve further to $z = z_3$. Finally, at $z = z_3$, we switch off the longitudinal modulation and continue its evolution in the nonlinear medium. The dynamical evolutions in both self-focusing ($\sigma = 1$) and defocusing ($\sigma = -1$) media are shown in Figs. 7 and 8, respectively.

One can see that in the absence of longitudinal modulation, the initial input exhibits oscillatory behavior from $z = 0$ to

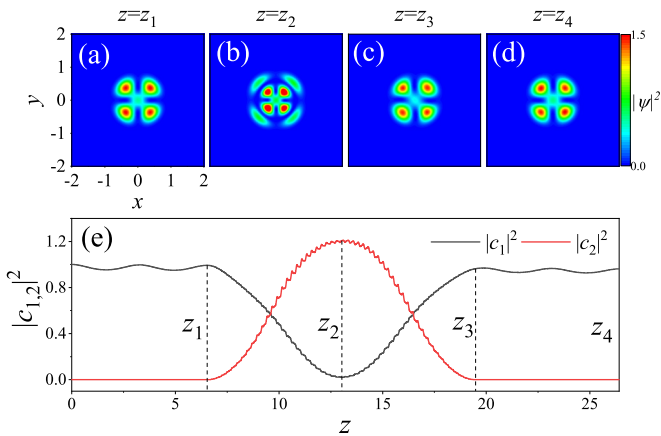


FIG. 7. Conversion between the sine modes $u_{02,s}$ and $u_{12,s}$ at $p_i = 2$ in a self-focusing medium. (a) Intensity distributions at $z = z_1$, z_2 , z_3 , and z_4 ; (b) corresponding evolution of the weights $|c_{1,2}(z)|^2$. Here, $\mu = 0$ as $0 \leq z < z_1$ and $z_3 < z \leq z_4$; $\mu = 0.1$ as $z_1 \leq z \leq z_3$, and $z_1 = 6.535$, $z_2 = 13.028$, $z_3 = 19.486$, $z_4 = 26.411$, $\sigma = 1$, and the other parameters are the same as those in Fig. 4.

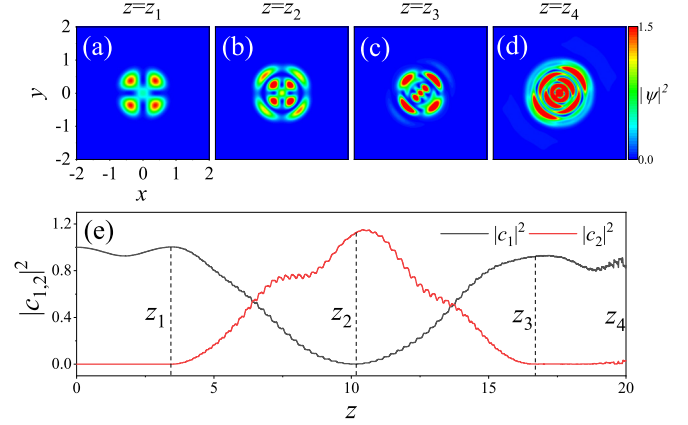


FIG. 8. Conversion between the sine modes $u_{02,s}$ and $u_{12,s}$ at $p_i = 2$ in defocusing medium. (a) Intensity distributions at $z = z_1$, z_2 , z_3 and z_4 ; (b) corresponding evolution of the weights $|c_{1,2}(z)|^2$. Here, $\mu = 0$ as $0 \leq z < z_1$ and $z_3 < z \leq z_4$; $\mu = 0.1$ as $z_1 \leq z \leq z_3$, and $z_1 = 3.435$, $z_2 = 10.183$, $z_3 = 16.702$, $z_4 = 20$, $\sigma = -1$, and the other parameters are the same as those in Fig. 4.

$z = z_1$ under the influence of nonlinearity [see Figs. 7(e) and 8(e)]. Here, z_1 is chosen as the point of maximum oscillation since its shape at $z = z_1$ closely resembles the initial profile, as shown in Figs. 7(a) and 8(a). Upon introducing resonant longitudinal modulation at $z = z_1$, the weight $|c_1(z)|^2$ decreases until it reaches its minimum value at $z = z_2$, indicating the conversion from $u_{02,s}$ to $u_{12,s}$, as shown in Figs. 7(b) and 8(b). With further propagation, $|c_1(z)|^2$ increases while $|c_2(z)|^2$ decreases until it reaches its minimum value at $z = z_3$; however, the scenario is different. For the self-focusing medium, it does not fully return to the initial profile at $z = z_3$, but after switching off the longitudinal modulation at $z = z_3$, it returns fully back to the initial profile at $z = z_4$ due to its oscillatory behavior, as shown in Figs. 7(c) and 7(d). However, for the defocusing medium, it cannot return back to the initial profile, as shown in Figs. 8(c) and 8(d).

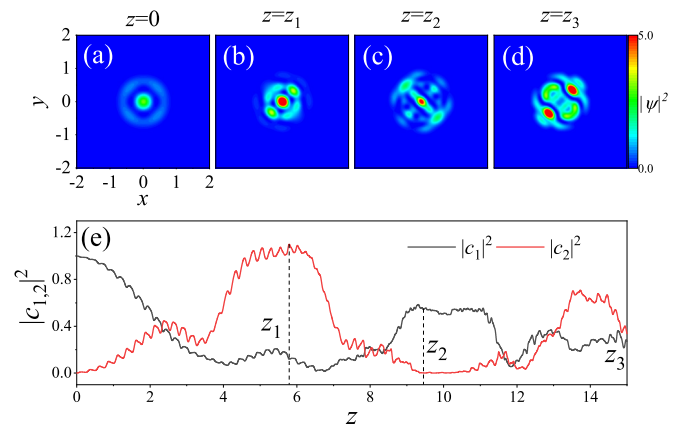


FIG. 9. Conversion between the basic modes u_{10} and u_{20} at $p_i = 2$ in the self-focusing medium. (a) Intensity distributions at $z = 0$, z_1 , z_2 and z_3 ; (b) corresponding evolution of the weights $|c_{1,2}(z)|^2$. Here, $\mu = 0.1$ as $0 \leq z < z_2$; $\mu = 0$ as $z > z_2$, and $z_1 = 5.792$, $z_2 = 9.452$, $z_3 = 15$, $\sigma = 1$, $\phi = 0$, and the other parameters are the same as those in Fig. 5.

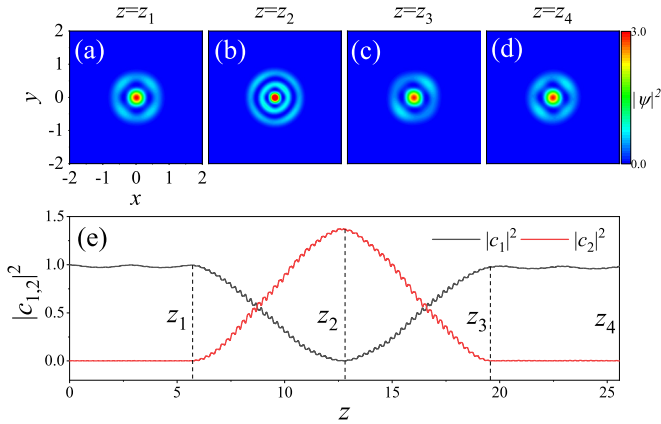


FIG. 10. Conversion between the basic modes u_{10} and u_{20} at $p_i = 2$ in the defocusing medium. (a) Intensity distributions at $z = z_1, z_2, z_3$, and z_4 ; (b) corresponding evolution of the weights $|c_{1,2}(z)|^2$. Here, $\mu = 0$ as $0 \leq z < z_1$ and $z_3 < z \leq z_4$; $\mu = 0.1$ as $z_1 \leq z \leq z_3$, and $z_1 = 5.725, z_2 = 12.810, z_3 = 19.569, z_4 = 25.567, \sigma = -1, \phi = 0$, and the other parameters are the same as those in Fig. 5.

Additionally, we demonstrated the conversion dynamics of the basic modes u_{10} and u_{20} under the action of longitudinal modulation for different nonlinear effects, as shown in Figs. 9 and 10. Here, we use u_{10} as the initial input and set the longitudinal modulation frequency to be $\Omega = \beta_{10} - \beta_{20}$. Notably, there is no mode conversion between the basic modes u_{10} and u_{20} in the nonlinear self-focusing medium, as shown in Fig. 9.

However, in defocusing medium, mode conversion can occur, as shown in Fig. 10. Similar to the mode conversion between the sine modes $u_{02,s}$ and $u_{12,s}$ in the self-focusing medium (see Fig. 7), the initial input u_{10} exhibits little oscillation from $z = 0$ to $z = z_1$ under the influence of nonlinearity, as shown in Figs. 10(a) and 10(e). With the introduction of resonant longitudinal modulation at $z = z_1$, it undergoes a conversion and transforms into u_{20} at $z = z_2$, where $|c_1(z)|^2$ reaches its minimum value [see Fig. 10(b)]. Subsequently, $|c_1(z)|^2$ increases while $|c_2(z)|^2$ decreases until $|c_2(z)|^2$ reaches its minimum value at $z = z_3$. However, at the position, it has not fully returned to the initial profile [see Fig. 10(c)]. Only upon switching off the longitudinal modulation does it return back to the initial profile at the point of maximum oscillation [see Fig. 10(d)].

It should be emphasized that in the above results, we first demonstrated the evolution dynamics of liner eigenmodes in the presence of nonlinearity and found that the sine

quadrupole modes and the basic modes with ring structure display oscillatory behavior in self-focusing and defocusing media, respectively. This means that they can attain a dynamic equilibrium between the nonlinearity and complex potential during propagation, resulting in the occurrence of conversion when resonant longitudinal modulation is introduced. However, the sine quadrupole modes in defocusing medium, as well as basic modes in self-focusing medium, are unable to achieve this dynamic balance, and as a result, conversion does not take place.

V. CONCLUSIONS

In conclusion, we have investigated resonant mode conversions in partially parity-time-symmetric multimode waveguides under the action of longitudinal periodic modulation. First, the linear version of the system was numerically solved, and the symmetry breaking and degeneracy splitting of linear eigenmodes in the complex waveguides were discussed in detail. The results have shown that, with the presence of gain/loss, the symmetry of degenerate dipole and hexapole eigenmodes is always broken, while the degenerate cosine and sine quadrupole eigenmodes will split, where the cosine modes retain their symmetry and topological charge, and the sine modes have zero topological charge and merge with the adjacent basic modes at a critical point. Based on these characteristics and with the aid of resonant coupled mode theory with a biorthogonality condition, mode conversions in the nonconservative system have been demonstrated. The results have shown that, under the resonance condition, conversions between the unbroken modes with the same topological charge and equal parity can occur, and the numerical and analytical results are in good agreement. Finally, the influence of nonlinear effects on the mode conversions was also discussed. The results have found that the mode conversions depend on dynamic equilibrium of the modes in nonlinear media, resulting in the conversions between the sine quadrupole modes in the self-focusing medium, as well as the basic modes with ring structure in the defocusing medium, being achieved. These results are beneficial for our further understanding of mode conversions in complex waveguides and can be applied to manipulation of the optical beam.

ACKNOWLEDGMENTS

This research was supported by the National Natural Science Foundation of China (Grant No. 11705108), 111 project (Grant No. D18001), and the Hundred Talent Program of the Shanxi Province (2018).

- [1] C. M. Bender and S. Boettcher, Real spectra in non-Hermitian Hamiltonians having \mathcal{PT} symmetry, *Phys. Rev. Lett.* **80**, 5243 (1998).
- [2] C. M. Bender, Making sense of non-Hermitian Hamiltonians, *Rep. Prog. Phys.* **70**, 947 (2007).
- [3] A. Ruschhaupt, F. Delgado, and J. G. Muga, Physical realization of \mathcal{PT} -symmetric potential scattering in a planar slab waveguide, *J. Phys. A: Math. Gen.* **38**, L171 (2005).

- [4] R. El-Ganainy, K. G. Makris, D. N. Christodoulides, and Z. H. Musslimani, Theory of coupled optical \mathcal{PT} -symmetric structures, *Opt. Lett.* **32**, 2632 (2007).
- [5] Z. H. Musslimani, K. G. Makris, R. El-Ganainy, and D. N. Christodoulides, Optical solitons in \mathcal{PT} periodic potentials, *Phys. Rev. Lett.* **100**, 030402 (2008).
- [6] A. Guo, G. J. Salamo, D. Duchsne, R. Morandotti, M. Volatier-Ravat, V. Aimez, G. A. Siviloglou, and D. N. Christodoulides,

- Observation of \mathcal{PT} -symmetry breaking in complex optical potentials, *Phys. Rev. Lett.* **103**, 093902 (2009).
- [7] C. E. Rüter, K. G. Makris, R. El-Ganainy, D. N. Christodoulides, M. Segev, and D. Kip, Observation of parity–time symmetry in optics, *Nat. Phys.* **6**, 192 (2010).
- [8] A. A. Zyablovsky, A. P. Vinogradov, A. A. Pukhov, A. V. Dorofeenko, and A. A. Lisyansky, \mathcal{PT} -symmetry in optics, *Phys.-Usp.* **57**, 1063 (2014).
- [9] K. G. Makris, R. El-Ganainy, D. N. Christodoulides, and Z. H. Musslimani, Beam dynamics in \mathcal{PT} symmetric optical lattices, *Phys. Rev. Lett.* **100**, 103904 (2008).
- [10] H. Ramezani, T. Kottos, R. El-Ganainy, and D. N. Christodoulides, Unidirectional nonlinear \mathcal{PT} -symmetric optical structures, *Phys. Rev. A* **82**, 043803 (2010).
- [11] A. A. Sukhorukov, Z. Xu, and Y. S. Kivshar, Nonlinear suppression of time reversals in \mathcal{PT} -symmetric optical couplers, *Phys. Rev. A* **82**, 043818 (2010).
- [12] R. Driben and B. A. Malomed, Stability of solitons in parity-time-symmetric couplers, *Opt. Lett.* **36**, 4323 (2011).
- [13] F. K. Abdullaev, V. V. Konotop, M. Öggen, and M. P. Sørensen, Zeno effect and switching of solitons in nonlinear couplers, *Opt. Lett.* **36**, 4566 (2011).
- [14] N. V. Alexeeva, I. V. Barashenkov, A. A. Sukhorukov, and Y. S. Kivshar, Optical solitons in \mathcal{PT} -symmetric nonlinear couplers with gain and loss, *Phys. Rev. A* **85**, 063837 (2012).
- [15] U. Al Khawaja, S. M. Al-Marzoug, H. Bahlouli, and Y. S. Kivshar, Unidirectional soliton flows in \mathcal{PT} -symmetric potentials, *Phys. Rev. A* **88**, 023830 (2013).
- [16] R. Li, P. Li, and L. Li, Asymmetric optical amplifier based on parity-time symmetry, *Proc. Rom. Acad., Ser. A* **14**, 121 (2013).
- [17] I. V. Barashenkov, D. A. Zezyulin, and V. V. Konotop, Jamming anomaly in \mathcal{PT} -symmetric systems, *New J. Phys.* **18**, 075015 (2016).
- [18] N. V. Alexeeva, I. V. Barashenkov, and Y. S. Kivshar, Solitons in \mathcal{PT} -symmetric ladders of optical waveguides, *New J. Phys.* **19**, 113032 (2017).
- [19] L. Morales-Molina and E. Aguilera-Valdés, Photon-assisted tunneling resonantly extending the domain of the \mathcal{PT} -symmetric phase, *Phys. Rev. A* **108**, 042205 (2023).
- [20] V. V. Konotop, J. Yang, and D. A. Zezyulin, Nonlinear waves in \mathcal{PT} -symmetric systems, *Rev. Mod. Phys.* **88**, 035002 (2016).
- [21] Y. Zhang, H. Zhong, M. R. Beli, Y. Zhu, W. Zhong, Y. Zhang, D. N. Christodoulides, and M. Xiao, \mathcal{PT} symmetry in a fractional Schrödinger equation, *Laser Photonics Rev.* **10**, 526 (2016).
- [22] Ş. K. Özdemir, S. Rotter, F. Nori, and L. Yang, Parity–time symmetry and exceptional points in photonics, *Nat. Mater.* **18**, 783 (2019).
- [23] H. Li, A. Mekawy, A. Krasnok, and A. Alù, Virtual parity-time symmetry, *Phys. Rev. Lett.* **124**, 193901 (2020).
- [24] S. Xia, D. Kaltsas, D. Song, I. Komis, J. Xu, A. Szameit, H. Buljan, K. G. Makris, and Z. Chen, Nonlinear tuning of \mathcal{PT} symmetry and non-Hermitian topological states, *Science* **372**, 72 (2021).
- [25] M. N. Akhter, S. B. Ivars, M. Botey, R. Herrero, and K. Staliunas, Non-Hermitian mode cleaning in periodically modulated multimode fibers, *Phys. Rev. Lett.* **131**, 043604 (2023).
- [26] J. Yang, Partially \mathcal{PT} symmetric optical potentials with all-real spectra and soliton families in multidimensions, *Opt. Lett.* **39**, 1133 (2014).
- [27] J. Yang, Symmetry breaking of solitons in two-dimensional complex potentials, *Phys. Rev. E* **91**, 023201 (2015).
- [28] Y. V. Kartashov, V. V. Konotop, and L. Torner, Topological states in partially- \mathcal{PT} -symmetric azimuthal potentials, *Phys. Rev. Lett.* **115**, 193902 (2015).
- [29] C. Huang and L. Dong, Stable vortex solitons in a ring-shaped partially- \mathcal{PT} -symmetric potential, *Opt. Lett.* **41**, 5194 (2016).
- [30] H. Wang, J. Huang, X. Ren, Y. Weng, D. Mihalache, and Y. He, Families of dipole solitons in self-defocusing Kerr media and partial parity–time-symmetric optical potentials, *Rom. J. Phys.* **63**, 205 (2018).
- [31] Y. Xue, C. Hang, Y. He, Z. Bai, Y. Jiao, G. Huang, J. Zhao, and S. Jia, Experimental observation of partial parity-time symmetry and its phase transition with a laser-driven cesium atomic gas, *Phys. Rev. A* **105**, 053516 (2022).
- [32] Y. V. Kartashov, L. Torner, and V. A. Vysloukh, Parametric amplification of soliton steering in optical lattices, *Opt. Lett.* **29**, 1102 (2004).
- [33] Y. V. Kartashov, A. Szameit, V. A. Vysloukh, and L. Torner, Light tunneling inhibition and anisotropic diffraction engineering in two-dimensional waveguide arrays, *Opt. Lett.* **34**, 2906 (2009).
- [34] Y. V. Kartashov, V. A. Vysloukh, and L. Torner, Enhancement and inhibition of light tunneling mediated by resonant mode conversion, *Opt. Lett.* **39**, 933 (2014).
- [35] Z. Yu and S. Fan, Complete optical isolation created by indirect interband photonic transitions, *Nat. Photon.* **3**, 91 (2009).
- [36] R. W. Robinett, Quantum wave packet revivals, *Phys. Rep.* **392**, 1 (2004).
- [37] I. L. Garanovich, S. Longhi, A. A. Sukhorukov, and Y. S. Kivshar, Light propagation and localization in modulated photonic lattices and waveguides, *Phys. Rep.* **518**, 1 (2012).
- [38] S. Longhi, Quantum-optical analogies using photonic structures, *Laser Photonics Rev.* **3**, 243 (2009).
- [39] K. O. Hill, B. Malo, K. Vineberg, F. Bilodeau, D. C. Johnson, and I. Skinner, Efficient mode conversion in telecommunication fiber using externally written gratings, in *Optical Society of America Annual Meeting* (Optica, Boston, Massachusetts United States, 1990), p. TuRR2.
- [40] K. S. Lee and T. Erdogan, Fiber mode coupling in transmissive and reflective tilted fiber gratings, *Appl. Opt.* **39**, 1394 (2000).
- [41] Y. V. Kartashov, V. A. Vysloukh, and L. Torner, Resonant mode oscillations in modulated waveguiding structures, *Phys. Rev. Lett.* **99**, 233903 (2007).
- [42] V. A. Vysloukh, Y. V. Kartashov, and K. Staliunas, Efficient mode conversion in guiding structures with longitudinal modulation of nonlinearity, *Opt. Lett.* **40**, 4631 (2015).
- [43] X. Zhang, F. Ye, Y. V. Kartashov, and X. Chen, Rabi oscillations and stimulated mode conversion on the subwavelength scale, *Opt. Express* **23**, 6731 (2015).
- [44] M. Ornigotti, G. D. Valle, T. T. Fernandez, A. Coppa, V. Foglietti, P. Laporta, and S. Longhi, Visualization of two-photon Rabi oscillations in evanescently coupled optical waveguides, *J. Phys. B: At., Mol. Opt. Phys.* **41**, 085402 (2008).

- [45] K. G. Makris, D. N. Christodoulides, O. Peleg, M. Segev, and D. Kip, Optical transitions and Rabi oscillations in waveguide arrays, *Opt. Express* **16**, 10309 (2008).
- [46] K. Shandarova, C. E. Rüter, D. Kip, K. G. Makris, D. N. Christodoulides, O. Peleg, and M. Segev, Experimental observation of Rabi oscillations in photonic lattices, *Phys. Rev. Lett.* **102**, 123905 (2009).
- [47] V. A. Vysloukh and Y. V. Kartashov, Resonant mode conversion in the waveguides with unbroken and broken \mathcal{PT} symmetry, *Opt. Lett.* **39**, 5933 (2014).
- [48] G. K. L. Wong, M. S. Kang, H. W. Lee, F. Biancalana, C. Conti, T. Weiss, and P. S. J. Russell, Excitation of orbital angular momentum resonances in helically twisted photonic crystal fiber, *Science* **337**, 446 (2012).
- [49] Y. V. Kartashov, V. A. Vysloukh, and L. Torner, Dynamics of topological light states in spiraling structures, *Opt. Lett.* **38**, 3414 (2013).
- [50] Y. Zhang, R. Wang, H. Zhong, J. Zhang, M. R. Belić, and Y. Zhang, Resonant mode conversions and Rabi oscillations in a fractional Schrödinger equation, *Opt. Express* **25**, 32401 (2017).
- [51] Y. Zhang, Y. V. Kartashov, Y. Zhang, L. Torner, and D. V. Skryabin, Resonant edge-state switching in polariton topological insulators, *Laser Photonics Rev.* **12**, 1700348 (2018).
- [52] H. Zhong, Y. V. Kartashov, Y. Zhang, D. Song, Y. Zhang, F. Li, and Z. Chen, Rabi-like oscillation of photonic topological valley Hall edge states, *Opt. Lett.* **44**, 3342 (2019).
- [53] K. Jin, Y. Li, F. Li, M. R. Belic, Y. Zhang, and Y. Zhang, Rabi oscillations of azimuthons in weakly nonlinear waveguides, *Adv. Photonics* **2**, 046002 (2020).
- [54] D. Wang, L. Li, and Y. Wang, Azimuthons induced by degenerate linear eigenmodes and their conversions under nonlinear modulation, *Opt. Express* **31**, 30783 (2023).
- [55] P. Griffin, P. Nagel, and R. D. Koshel, The planewave expansion method, *J. Math. Phys.* **15**, 1913 (1974).
- [56] D. C. Brody, Biorthogonal quantum mechanics, *J. Phys. A: Math. Theor.* **47**, 035305 (2014).
- [57] G. S. Agarwal, Rotating-wave approximation and spontaneous emission, *Phys. Rev. A* **4**, 1778 (1971).